Fuel 241 (2019) 941–953

Contents lists available at ScienceDirect

Fuel

journal homepage: www.elsevier.com/locate/fuel

Full Length Article

Effect of electric charge and temperature on the near-field atomization of diesel and biodiesel

G. Singh[a], P.X. Pham[a,b], A. Kourmatzis[a,*], A.R. Masri[a]

[a] School of Aerospace, Mechanical and Mechatronic Engineering, The University of Sydney, NSW 2006, Australia
[b] Department of Internal Combustion Engine, Le Quy Don Technical University, Hanoi, Viet Nam

ARTICLE INFO

Keywords:
Electrostatic atomization
Biodiesels
Primary atomization

ABSTRACT

High speed backlight imaging combined with particle tracking velocimetry is used to analyse the near-field characteristics of a series of typical charge injection atomizer sprays. Diesel and biodiesels are studied as a function of applied voltage and temperature, in order to provide new information on the influence of fuel preheating on charged sprays. Detailed quantitative characterisation of ligament and droplet statistics, fragment orientation and local dimensionless scalings using "effective surface tension" are presented. These shed new light on the fragmentation mechanisms that drive primary atomization in charge injection systems. It is observed that pre-heating can reduce the droplet size of electrostatically atomized dielectric fluids. However, the advantage of pre-heating is limited by a higher ionic mobility at higher temperatures which increases the leakage current. Bimodality in the droplet size distribution is noted which confirms previous work, and this study extends the literature by analysing distributions of ligament size. Statistics of orientation and velocity of arbitrarily shaped ligament-like fragments are presented to quantify the oscillatory nature of the primary atomization zone. Analysis of the local non-dimensional Weber number using an effective surface tension demonstrates that at a critical applied voltage, atomizing arbitrarily shaped fragments approach a local critical Weber number value ($We^{1/2} \sim 0.8$) which is comparable to previous work done in non-charged laminar and air assisted sprays.

1. Introduction

Atomization is generally understood to be governed by jet instabilities that can promote liquid breakup, complemented by turbulence in the liquid jet core [1–4]. The effects of instabilities on atomization have been characterised in the past in terms of non-dimensional parameters such as the Weber number (We), Reynolds number (Re) and Ohnesorge number (Oh) and it is generally known that the spray structure and breakup regime is a function of these non-dimensional numbers [1,2].

Electric charge can promote atomization due to Coulombic repulsion, but also potentially due to electro-convective turbulence [5–7], and has the potential to be substantially more efficient compared to either pressurized liquid or air assistance [5,30]. Electrostatic atomization of electrically insulating liquids can result in small droplets with a narrow droplet size distribution [8,9]. The use of dielectric liquids, such as diesel, biodiesel, Kerosene and other fuels to generate electrostatic sprays has expanded the potential applications of electro-hydrodynamic (EHD) sprays to microscale turbines, microscale cooling, painting, printing, agriculture, and many other spraying systems [10–12,5].

Most of the literature on electrified sprays refers to work on conducting and semi-conducting liquids [5,13,14]. Here, the focus is on charge injection atomizers, which spray dielectric electrically insulating liquids. Such a charge injection atomization system consists of two key components: a negative electrode (generally a needle or small diameter cylinder), and an orifice plate or nozzle that operates as a ground electrode [5,9,8,6]. Charge is introduced into the liquid jet by forcing liquid through an inter-electrode gap and out of the orifice. The amount of charge introduced is proportional to the Coulomb force that is responsible for atomizing the liquid jet and the literature has reported that inter-electrode gap (l), and nozzle diameter (D), are two important parameters that govern the electrical performance of the spray [15,5,7,9]. Owing to extensive work on charged injector optimization, the literature on the effect of l/D and other key parameters on spray electrical characteristics is in a relatively advanced state. For a thorough review of electrostatic atomizers and related theory the reader is directed to Shrimpton [5], where here only a brief review of key relevant findings is presented.

A number of studies have examined charged droplet size

* Corresponding author.
E-mail address: agisilaos.kourmatzis@sydney.edu.au (A. Kourmatzis).

https://doi.org/10.1016/j.fuel.2018.12.090
Received 24 September 2018; Received in revised form 14 December 2018; Accepted 18 December 2018

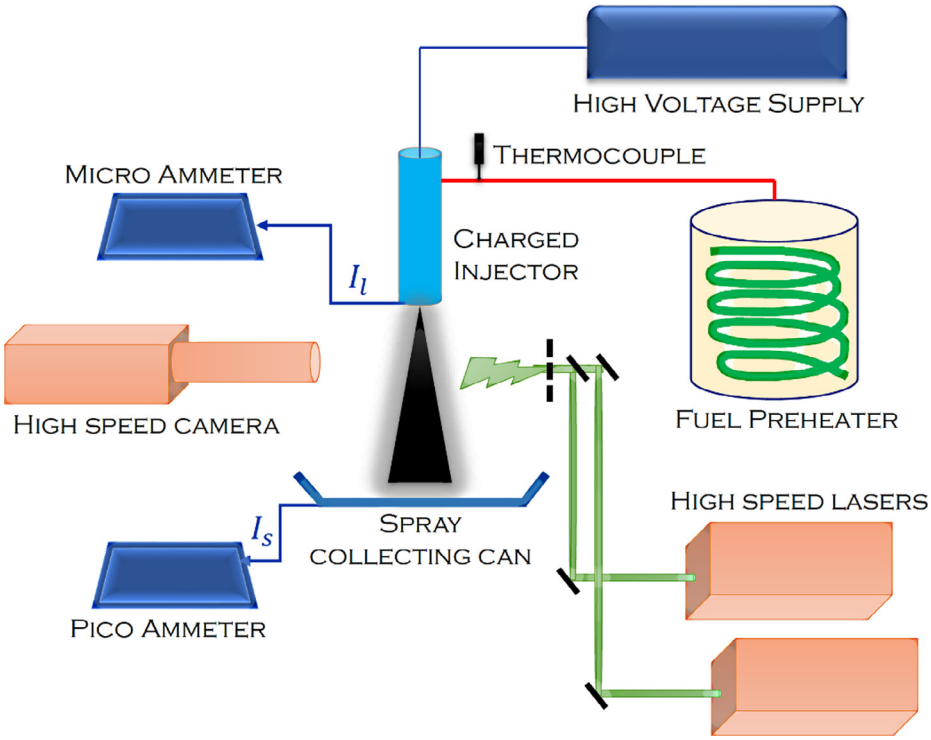

Fig. 1. Outline of experimental setup.

characterization with phase Doppler anemometry [5,16,6,31] and with high speed microscopic imaging [4,17,3,18]. Key reported features are a generally bimodal droplet size distribution at lower charge levels [5] which can shift to a conventional monomodal distribution with a lower mean droplet size at higher levels of charge and inter-phase mixing [18,7,19]. In addition to size distributions, Shrimpton [9,15] reports data on global break-up length as a function of charge on the spray and this is complemented by thorough electrical characterisation of EHD sprays with respect to the current in the spray and that leaked to the atomizer housing. Such measurements have identified the now well established "super-critical" regime where the spray current reaches a peak, prior to a decrease, which is said to occur due to corona discharge in the primary atomization zone [5]. The "sub-critical" regime refers to a maximum charge level, which is followed by a breakdown in the inter-electrode gap [5]. Along with conventional fuels, studies have also demonstrated the capacity of charge injection atomization to work effectively for fuels with a wide range of viscosities, such as vegetable oils [8]. Ahmad et al. and Malkawi et al. [16,8] observed the electro-spinning phenomenon in charged sprays (as observed in polymer manufacturing) which is due to a repulsive Coulomb force acting on viscous liquids to promote helical movement of a stretched liquid jet.

Unlike in conventional pressure or air-assisted sprays, electrostatic atomization can be governed by a combination of electrical forces, hydrodynamic characteristics (e.g. liquid jet turbulence), and aerodynamic characteristics (interfacial instabilities). Therefore, some additional parameters are needed to study its distinct behaviour. Recently, Kourmatzis and Shrimpton [6] formulated an electric jet Reynolds number (Re_{Ej}) to represent the ratio of electro-inertial force to viscous force. Re_{Ej} employs ionic mobility and electric field to re-define the velocity scale as an ionic drift term instead of jet velocity. It was reported that the conventional electric Reynolds number (Re_E), defined as the ratio of electro-inertial to viscous forces in the inter-electrode gap, varies linearly with the jet Reynolds number. This implies a link between the inter-electrode gap and the primary atomization zone [6]. Kourmatzis and Shrimpton [6] also reported that the surface tension of the liquid can be modelled to decrease with an increase in jet electric charge hence giving rise to an 'effective' liquid jet surface tension to account for this reduction, and offering an approach to account for the effect of electric charge in an aerodynamic scaling for primary atomization [7]. The reduced surface tension results in a high local Weber number, which indicates improved atomization probability in charged sprays. Such an approach followed from the original formulation of effective surface tension on charged droplets [5].

Charge injection atomizers would benefit significantly from robust correlations that can describe the relationships between applied voltage and current to droplet size. Such information which would assist the development of simple analytical design tools for charge injection atomizers, necessitates a better understanding of the near-field atomization region. Such studies are scarce in the field of charge injection atomization.

The application of any spraying technique can also be extended to heavy fluids by preheating the fuel, a process that can also be used in internal combustion engine applications [20,21,32]. Liquid preheating in the past has also been applied to highly viscous fluids in order to enable generation of a spray. Recently, Gorty et al. [22] have used electrostatic charge for spraying chocolate, where they preheated the chocolate to reduce its viscosity. They reported a successful electrostatically assisted spraying of chocolate at 35 °C, and at 50 °C with a droplet size ranging from 0.1 to 1000 μm. With a view to extend the charge injection technique to sustainable fuels such as biodiesel, preheated fuels are investigated in this contribution. To the authors' knowledge, there is no work that has been conducted to date which has quantitatively examined the influence of temperature on electrified dielectric liquid sprays.

This contribution aims to investigate the time resolved near-field structure of an electrostatic spray using a variety of fuels as a function of applied potential and temperature. Characterization techniques which have recently been applied to turbulent sprays will be implemented to a typical set of charge injection atomization conditions, with the overall objective being to shed new light on how near-field ligament sizes and dynamics are affected by electrostatic conditions at various temperatures. The paper begins with a brief discussion of the

experimental methodology and electrical characteristics of the fuels. This is followed by an analysis of near-field spray images to include ligament and droplet sizes and velocities as well as orientations measured using a validated high speed microscopic imaging method [23]. The paper concludes by examining some relevant local dimensionless numbers, by making use of the effective surface tension term, and comparing the findings to recent analysis of sprays in the Rayleigh break-up regime.

2. Experimental methodology

Fig. 1 outlines the experimental setup which includes a charge injection system, an imaging system and a current measurement system. The injection side consists of an electrostatic injector, a high voltage power supply, a fuel pre-heating system, and fuel delivery system. The imaging side incorporates (i) a high-speed camera coupled to a long-distance microscope and operated in PIV mode, (ii) two high-speed lasers run with a short time delay and (iii) optics to guide the laser beams. The current measurement system has an analogue micro-ammeter and a digital pico-ammeter to measure the leakage current and spray current respectively.

2.1. Injection system

Fig. 2 shows the schematic of the electrostatic spray injector used in this study. The injector has been developed in-house and is a typical plane-plane charge injector similar to previous studies [6]. It consists of a negatively charged cylindrical electrode (9) and an orifice plate (8) with a central-hole diameter of 0.25 mm which has been employed as a ground electrode. Both the negative and ground electrodes are made from brass. The normalized electrode gap (l/D) is maintained at 1.5 for all the experiments reported here but this is adjustable using a micrometer as shown in Fig. 2. The injector body is made from Perspex and allows optical access to visualize flow inside the injector, which is planned in the next phase of research. For more details on the injector design, the reader is directed elsewhere [24]. At the negative electrode, the voltage is supplied from a high voltage Spellman SL Series device. It has a range of 1–20 kV with 10 W power. A range of 0 to −15 kV has been used here.

A Genie Touch syringe pump is utilised to deliver fuel to the injector. The syringe pump has two cylinders of 60 mL capacity, each. Two flow rates have been investigated corresponding to a mean jet exit velocity of 5 m/s and 10 m/s.

All three fuels are preheated in an in-house developed heating system which consisted of a temperature-controlled propylene-glycol bath reaching temperatures of up to 150 °C. The fuel was delivered into the bath through a purpose designed copper coil. The temperature of the fuel is measured a few centimetres upstream of the orifice outlet of the injector using a K-type thermocouple. Three temperatures are investigated for all three fuels—fuel at a temperature of ~25 °C, at 40 °C, and at 70 °C.

2.2. Current measurement system

The charged spray is collected in an isolated metal container. The container is connected to a Pico-ammeter (Keithley Model 6485) with a

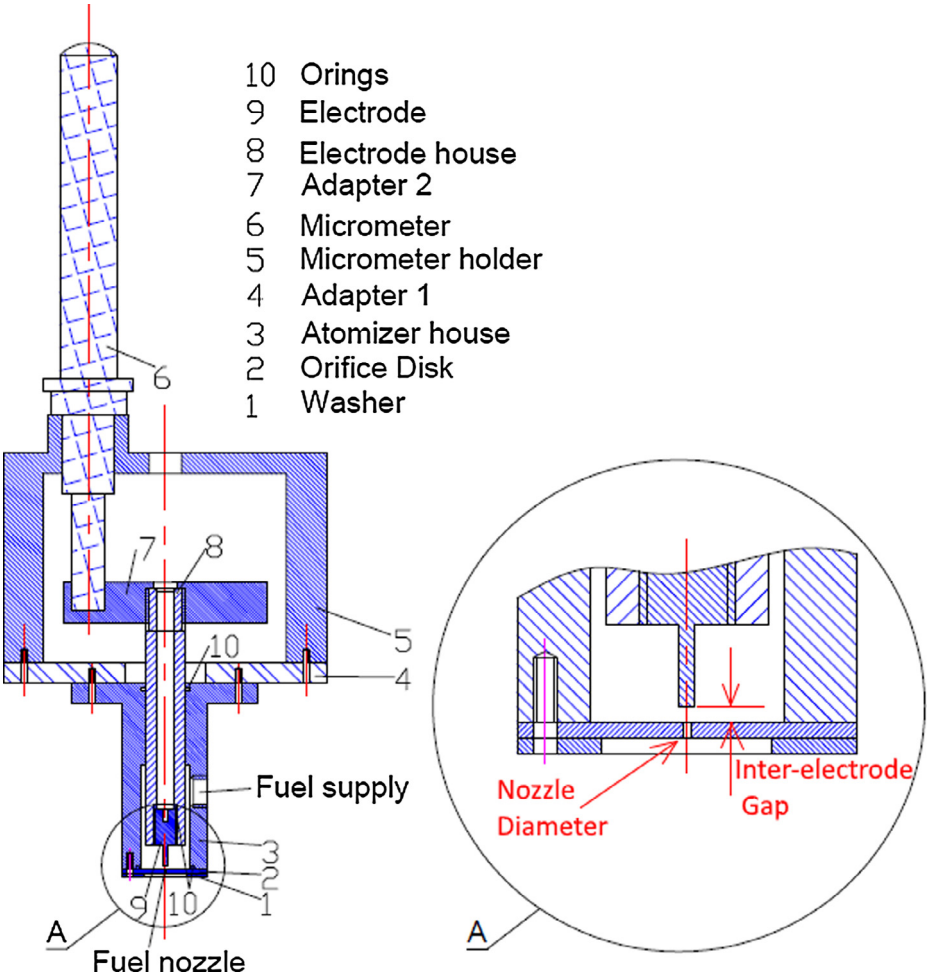

Fig. 2. Outline of electrostatic injector.

range of 10 fA to 20 mA and a data collection rate of 1000 Hz. A mean value of spray current is measured from the ammeter. The current leaking from spray to the ground electrode is measured using a micro-ammeter connected to the orifice plate. The micro-ammeter is a Simpson 04359 Tautband model, which has a range of 0 μA–10 μA with a resolution of 0.2 μA. The use of analogue ammeters was unavoidable for the leakage current measurements to prevent damage to sensitive equipment in the event of a dielectric breakdown occurrence.

2.3. Imaging system

High speed microscopic imaging, as illustrated in Fig. 1 is utilized to investigate the near-field structure of the spray. Images are captured by a high-speed camera (LaVision-High Speed Star 6) coupled with a QM100 long distance microscope. Two high-speed lasers (Edgewave high speed diode lasers, 5 kHz, 15 W) are guided through opal glass diffusing optics and used as a light source. A time delay of 20 μs is applied between the beams and the pulse pairs are timed with the two frames acquired from the High-speed PIV camera using a LaVISION high speed controller. The software DAVIS (version 8) is employed to control the imaging system and record the images to be exported to an in-house image processing code to be described below. Two axial locations are captured for each case, one at the onset of liquid jet breakup and one second position, approximately equal to one imaging frame (3 mm) downstream of the first.

2.3.1. Image characteristics and processing

Images are processed using an in-house developed MATLAB code. First, the images are binarized using a calibrated threshold image intensity to separate objects from the background. The threshold intensity is a critical parameter in image processing as a very low threshold rejects the small objects and a high threshold results in merging of two proximate objects. The literature has suggested that a threshold intensity in the range of 40–60% of the background intensity gives the best results with a maximum of 10% error in the object size, and this has been subject to extensive study by these authors in previous work [17,23,3]. Therefore, a threshold intensity in the range of 40–60% is adopted for binarizing all the images. The detailed image binarization and calibration technique which has been confirmed to accurately measure droplet size characteristics and physically reasonable results of non-spherical object statistics is discussed in detail elsewhere [3,23,17]. The binarized images are analysed using in-built image processing functions of MTALAB to get object size characteristics.

A total of 2000 image sets are captured for each location, with a single image set consisting of two image frames separated by a delay time (Δt) of 20 μs. Each image frame has a size-resolution of 768*768 pixels, which gives a square image size of 3.52*3.52 mm and a spatial resolution of 4.6 um/pixel. The two images of an image set are used to estimate the velocity of the objects using the principle of particle tracking velocimetry (PTV). Each particle is tracked in the two images to determine the distance travelled by it in a Δt time interval to calculate its velocity, as shown in Fig. 3. To measure the distance travelled by an object, its boundary is extracted and the difference between the highest points of the object-boundary in two frames is considered as the distance travelled by the object. A time interval of 20 μs between the two frames results in a velocity resolution of 0.23 m/s with a maximum error of 2%. The detailed PTV technique and its validation for velocity measurement of these types of un-atomized sprays is covered in detail elsewhere [23].

2.4. Fuels

Diesel and biodiesel fuels are investigated to enable some degree of variation in fuel properties as shown in Table 1. The experiments are performed with two biodiesels, named here as B3, and B4 of varying carbon chain length and saturation degree, and commercial diesel [25]. The relevant non-dimensional parameters such as jet exit Reynolds number ($Re = \rho UD/\mu$), Weber number ($We = \rho U^2 D/\sigma$), and Ohnesorge number ($Oh = \mu/\sqrt{\rho\sigma D}$), along with relevant fuel properties are listed in Table 1. Here, U is jet velocity, D is nozzle diameter, σ is surface tension, ρ is density, and μ is dynamic viscosity of the fluid. The electrical conductivities of these fuels were not measured directly however leakage current vs. voltage response indicates that fuels B3 and B4 behave very similarly to Diesel in the Ohmic charging region. We therefore expect all conductivities to be within the same order of magnitude and this is in agreement with previous work measuring electrical conductivities of vegetable oils and Diesel [16] and also aligns with the findings shown both in [24] but also in this contribution that indicate similar spray specific charge vs. voltage response among the fuels.

The electrical performance of these fuels is shown in Fig. 4 where the spray specific charge is plotted as a function of voltage for a mean injection velocity of 10 m/s. The spray specific charge (given in Coulomb/m^3) is the measured spray current divided by the volumetric flow-rate of the fuel. For both heated and unheated fuel, the specific charge increases with voltage for all three fuels as expected. For diesel and B3, the specific charge drops after attaining a peak value and this drop corresponds to the critical voltage 'Vc' as suggested in previous studies [5,16]. The critical voltages corresponding to each fuel and temperature are listed in Table 1. It is evident that the trend in the peak specific charge is consistent with viscosity such that B4 attains the maximum value of spray specific charge, followed by B3 and diesel.

It is observed that preheating the fuel results in a lower specific charge, which is consistent for all three fuels preheated to 40 °C and 70 °C, with an exception for B3 at 40 °C, where the specific charge does not drop significantly on preheating. However, the critical voltage for B3 drops from 8 kV at normal temperature to 5 kV at 40 °C, and 70 °C respectively. The reason for this trend could be attributed to a reduction in viscosity on preheating that results in an increased ionic drift, which can influence the ratio of leakage to spray current. The literature on charged injection with preheated fuels is very limited, however, similar trends for specific charge has been reported for preheated fluids in the food processing industry, where the electrical conductivity of the fluids dropped on preheating [22,26].

3. Results and discussion

The imaging results are discussed in three parts. The first part will discuss the near field structure of the spray through examining the onset of jet breakup and measured orientation of jets and fragments. The second part will discuss arbitrarily shaped fragment population statistics (sizes and velocities) by characterizing fragments into droplets and ligaments. The last part will discuss the effect of standard non-dimensional parameters on electrostatic spray atomization, and compare to the literature on Rayleigh break-up, for which all of the sprays shown in this contribution can be categorized under.

3.1. Near-field structure

Fig. 5 shows the near field images of diesel spray at two temperatures, (25 °C & 40 °C), at the onset of jet breakup, with a 10 m/s jet exit velocity. It is observed that the high specific charge at the critical voltage results in large oscillations, as expected, however, the variation in oscillations beyond the critical voltage (V > Vc) is minor. These results are also consistent for B3 and B4 although for B4, the oscillations increase continuously with voltage.

In a charge injection system, the spray oscillations are a function of charge content. Preheating the fuel reduces the charge content and therefore results in lower spray oscillations as compared to spray oscillations at normal temperature. This is evident in Fig. 5, where the spray jet oscillation is lower at 40 °C as compared to a jet at normal temperature. A detailed discussion on spray fluctuations, in terms of

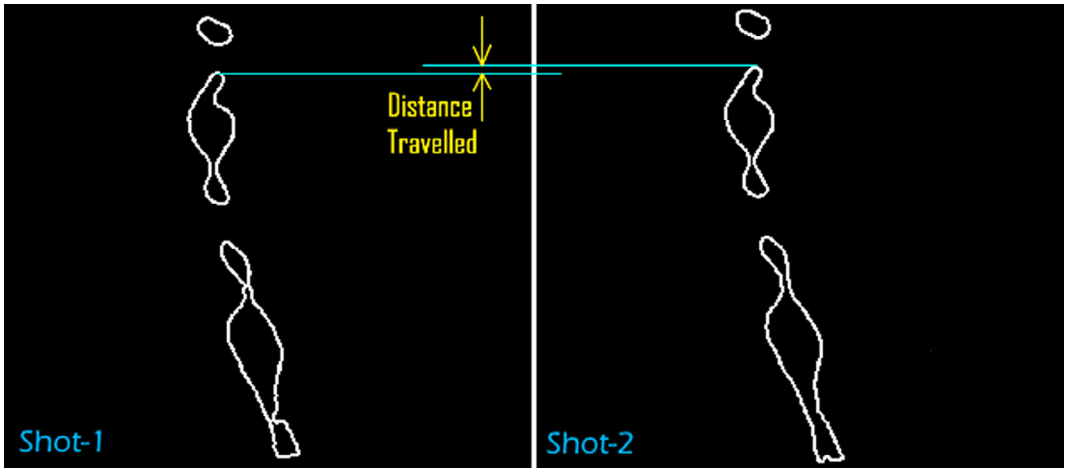

Fig. 3. Binarized image of two frames separated by a time interval of 20 μs. Figure shows tracking of an object in two frames to compute the distance travelled by it.

Table 1
Fuel properties with relevant non-dimensional numbers and critical voltages.

Properties	Diesel	B3 $C_{18.3}H_{35.3}O_2$	B4 $C_{18.7}H_{35.3}O_2$
C-Atom*	–	18.3	18.7
Density (kg/m^3)	848	873	879
Viscosity (mPa.s)	3.2	4.32	4.65
Surface Tension (mN/m)	23	29.9	29.9
Oh (×1000)	45	53	57
$Re_{JetExit}$ (10 m/s)	662	505	473
$We_{JetExit}$ (10 m/s)	1.3	1.0	1.0
V-Critical (25 °C) (kV)	5	8	–
V-Critical (40 °C) (kV)	5.5	6	–
V-Critical (70 °C) (kV)	5	6	–

* For detailed properties, refer [25,21].

fragment orientation, is discussed in the following section.

3.1.1. Orientation vs size

The orientation of liquid fragments and jet partly describes the nature of their oscillations. Malkawi et al. [8] and Rigit and Shrimpton [9] have reported study of liquid jet dynamics however this section presents quantitative data on near-field liquid jet and fragment oscillatory behaviour through measuring the orientation of each fragment in the population with respect to the nozzle axis. Only normal-temperature cases are discussed here as similar trends are observable for pre-heated fuel cases. The definition of orientation here is illustrated in the schematic of Fig. 5 showing fragments with respect to the nozzle tip, its axis and the horizontal plane. The liquid jet at the nozzle tip oscillates within the frame. For a given liquid fragment, as shown in Fig. 5, the major axis is shown with respect to the horizontal as well as the vertical axis of the nozzle. The orientation angle, θ is defined as the angle between the major axis of a fragment with respect to a horizontal plane, as shown in Fig. 6. A 90-degree orientation implies that the jet major axis is parallel to the direction of flow and a 0-degree orientation implies that the jet axis is perpendicular to the direction of flow or is perfectly radially oriented. For perfectly spherical objects, such as small droplets, the vertical axis is considered as the major axis, which results in a 90-degree orientation for these objects.

Fig. 7 (left column) shows a scatter plot of the absolute orientation

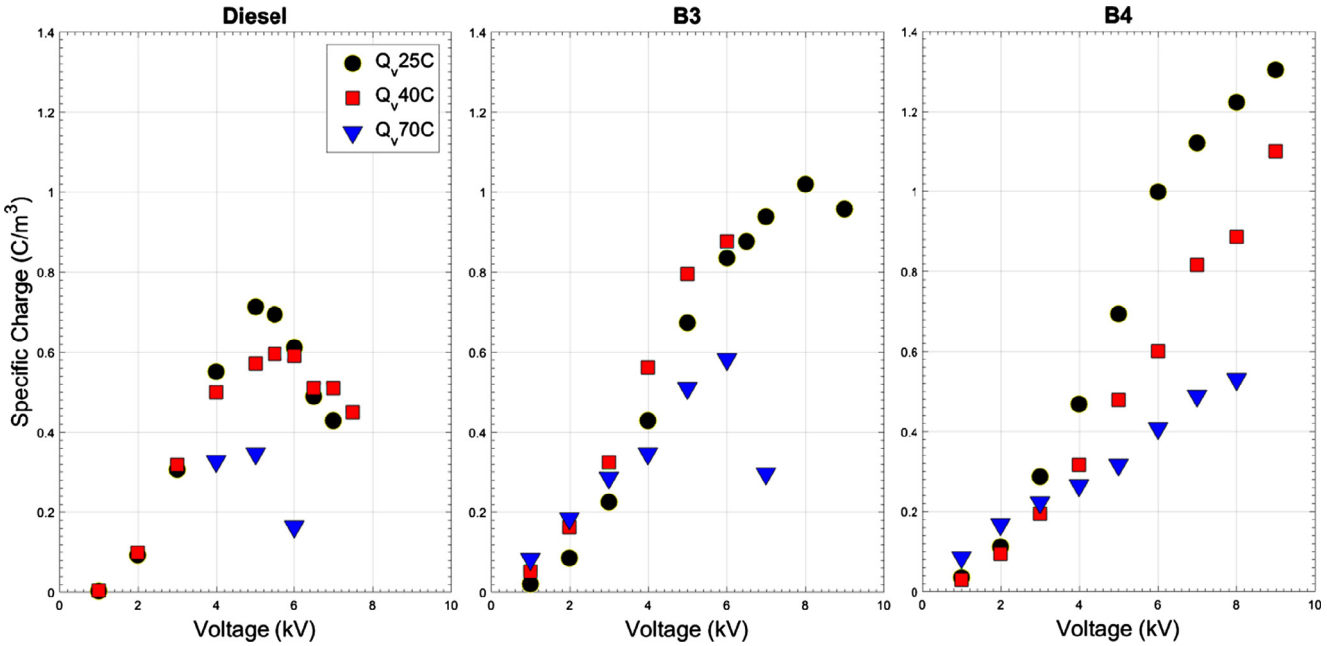

Fig. 4. Spray specific charge vs voltage of all three fuels with mean jet exit velocities corresponding to 10 m/s at a normal temperature, and at 40 °C(For B3 fuel, no measurements were taken after reaching critical voltage of 6 kV due to dielectric breakdown), and 70 °C.

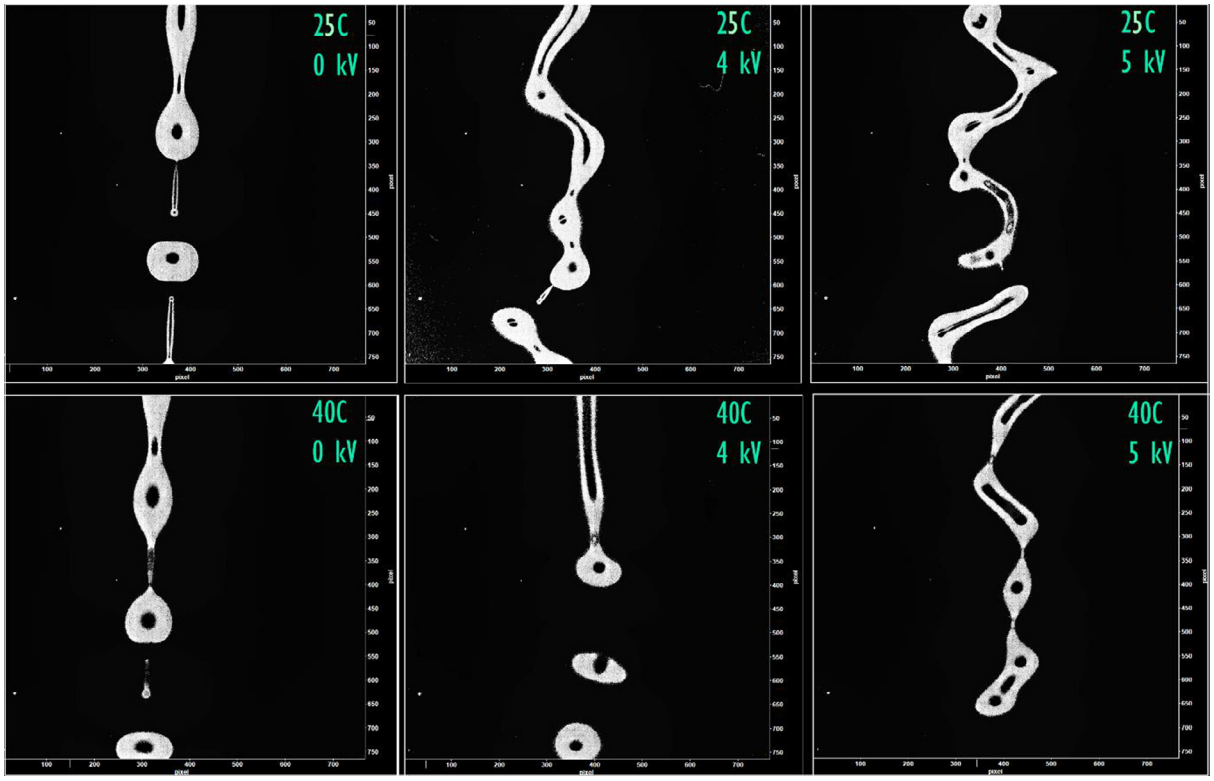

Fig. 5. Near field images of spray at the onset of jet breakup location for a range of voltages at a jet exit velocity of 10 m/s. Top three images are diesel at normal temperature, and bottom three are diesel at 40 °C. Rightmost images are at critical voltage. Frame size is approximately 3.5*3.5 mm.

of the liquid jet tip. It is evident from the figure that with an increase in voltage, for both diesel and B3, the jet tip orientation moves further away from 90-deg as shown in Fig. 6 indicating higher jet fluctuations at higher voltage. Past the critical voltage, the liquid jet can move away from an axial orientation completely, indicating that electrical forces are significant enough to completely radially bend the tip of the jet. This type of data is particularly useful for the quantitative validation and development of Volume of Fluid (VoF) models used for modelling electrostatic atomization. It also agrees with the electrospinning effect observed in previous studies, where the jet and liquid fragments can oscillate significantly [16,5,8].

Both B3 and diesel behaved similarly in terms of jet tip dynamics and therefore Fig. 7 (right column) shows the orientation of fragmented (atomized objects shedding from the liquid jet) as a function of their major axis for diesel only. It is noticed that the orientation of smaller objects, (d10 < 1 mm), mostly droplets, is scattered from −90-degree to +90-degree and this does not change with applied voltage. For all cases, the orientation of these small objects does not exhibit any trend, which is not surprising as these are constantly deforming and oscillating randomly, with an addition of charge not generally changing this.

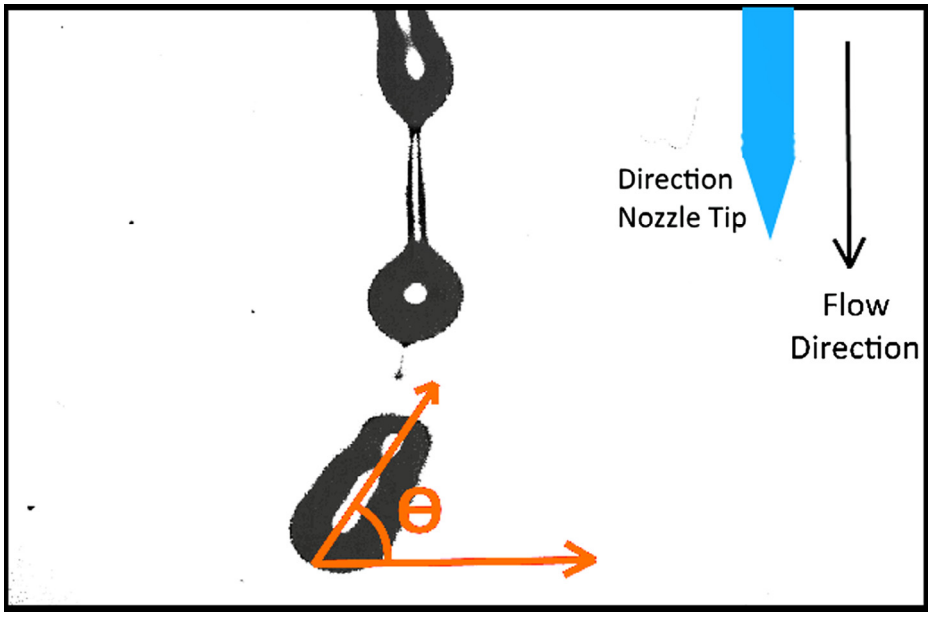

Fig. 6. Schematic for orientation of fragment with respect to direction of flow.

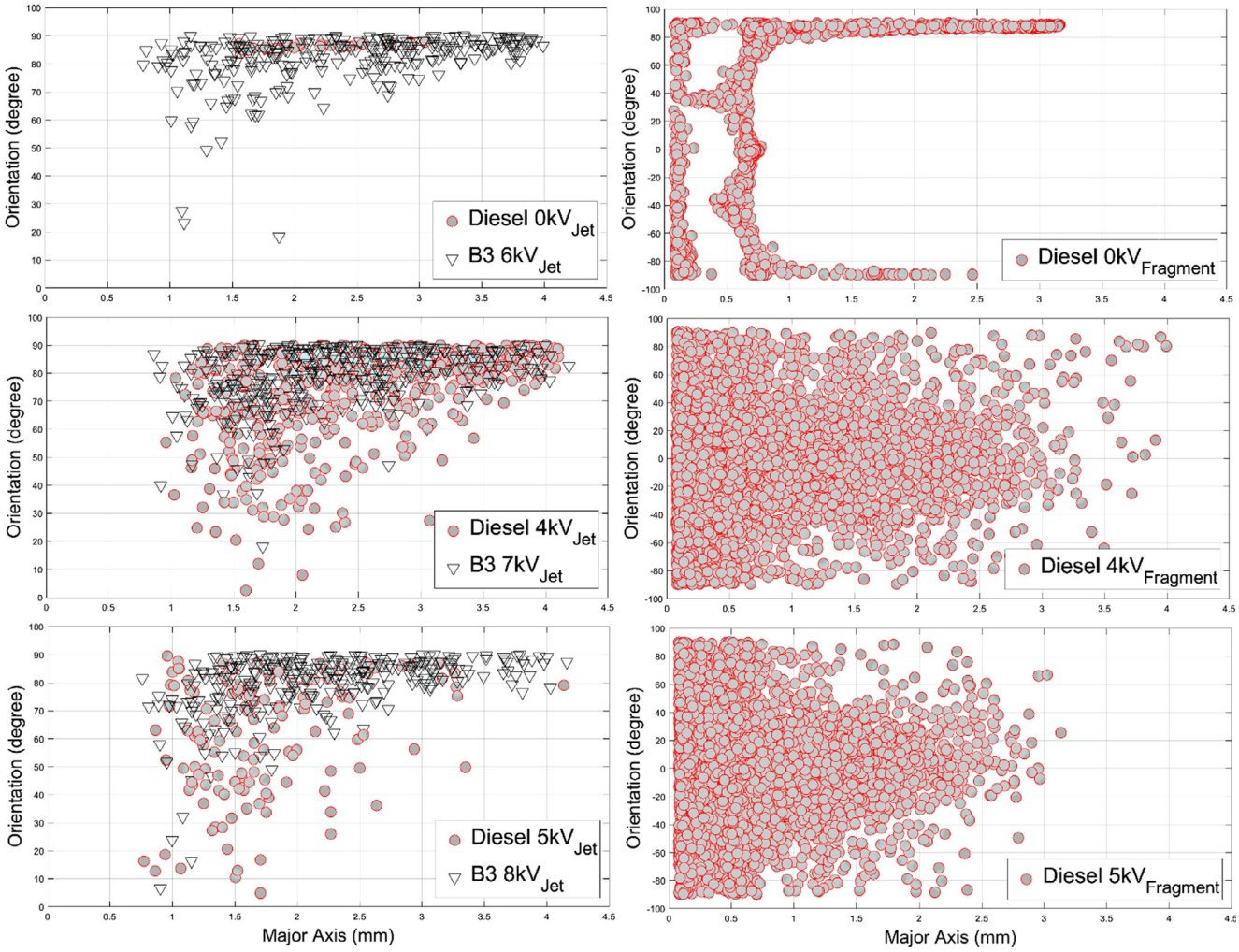

Fig. 7. Orientation of jet tip and fragments vs major axis for a jet exit velocity of 10 m/s. Left column shows the absolute value of orientation of jet tip of diesel and B3 for a range of voltage (from top to bottom, diesel – 0 kV, 4 kV, 5 kV and B3 – 6 kV, 7 kV, 8 kV). Right column shows the orientation of fragments of diesel spray for a range of voltages (from top to bottom, diesel – 0 kV, 4 kV, 5 kV).

However, the orientation of larger size objects (a major axis dimension of several liquid jet diameters) clearly moves towards 0-degrees with an increase in applied voltage showing a preferential re-orientation of ligaments with an increase in spray specific charge. For the no voltage (0 kV) case of diesel, a large proportion of large objects are at a 90-degree orientation, and this is indicative of a dripping mode Rayleigh breakup, where the jet does not fluctuate radially [2,1]. Both jet tip and fragment oscillations clearly increase with an increase in applied voltage. This suggests that charge induced electrical forces start to dominate over the aerodynamic forces, with the critical voltage (maximum spray specific charge) acting as a useful threshold to determine the extent of near-field fragment orientation and enhanced radial fluctuation of the spray.

3.1.2. Jet breakup length vs charge

In the literature spray break-up location has generally been determined using global images of the spray, which does not offer the degree of accuracy afforded by near-field imaging. The location of onset of jet breakup from the nozzle tip has been termed here as the jet breakup length. The jet breakup length is measured by analysing the images captured using the long-distance microscope. Two frames are captured, one at the onset of jet breakup (where the intact jet tip is first identified) and another one field of view downstream of it. Owing to large oscillations of the jet tip and limited frame size, a few breakup events are observed in the second frame, as shown in Fig. 8. Therefore, based on the jet tip appearance in each frame, a weighted average of the mean breakup location is calculated. Eq. (1) shows the calculated breakup length, where L_{jb} is the weighted average of mean jet tip location. L_{mf_1} and L_{mf_2} are the mean of jet tip locations in frames 1 and 2 respectively. N_{f2} and N_{f2} are the respective number of tip appearances in frames 1 and 2:

$$L_{jb} = \frac{L_{mf_1} N_{f1}}{N_{f1} + N_{f2}} + \frac{L_{mf_2} N_{f2}}{N_{f1} + N_{f2}} \quad (1)$$

The mean weighted jet breakup location is normalised by the jet diameter and is presented in Fig. 9. It is evident from the figure that the breakup location moves closer to the nozzle tip with an increase in specific spray charge. Preheating the fuel lowers the viscosity of the fuel [27,28] and can therefore promote earlier breakup of the jet, as shown in Fig. 9 for diesel and B3. As an example, for a fixed spray specific charge, for biodiesel B3, decreasing the temperature from 40 °C to 25 °C at a charge of ~0.8 C/m^3 results in a 40% increase in the break-up length. A similar effect is observed with diesel fuel at a charge of 0.6 C/m^3. While preheating the fuel does not change the electrostatic atomization nature of the spray, the reduced viscosity can therefore have a significant effect on the break-up location. While B4 also observes the trend of a decrease in break-up location with an increase in spray charge, the relationship with temperature is less clear, which is subject to further investigation.

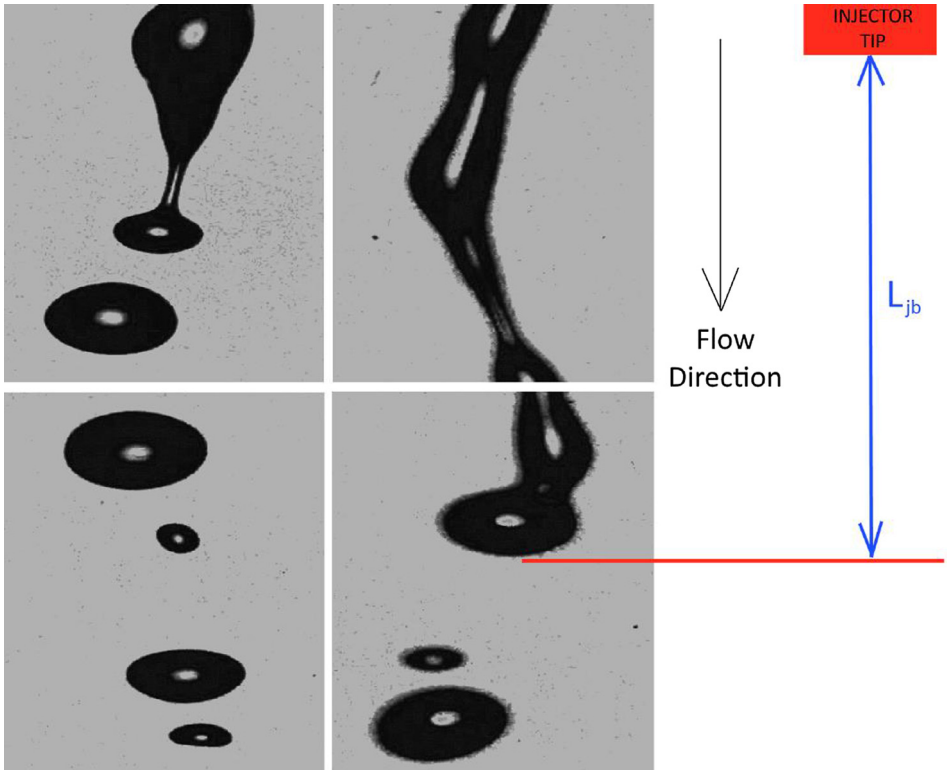

Fig. 8. Image showing breakup location in two different frames. Left, the breakup occurs in the first frame (top), where the liquid shed sheds a droplet. Right, the breakup occurs in the second or downstream frame (bottom).

3.2. Fragment population

Atomization of a jet results in objects or fragments of various size and shape such as ligaments (non-spherical objects) and droplets (spherical objects). The variation of fragment shape is more significant in the primary breakup or near-field region and therefore, a statistical study of these fragments must be characterized for a full understanding of the near-field zone. In this contribution, objects are classified in two major categories based on their aspect ratio. The spherical and slightly non-spherical objects (aspect ratio < = 3) are categorized as droplets. The non-spherical objects (aspect ratio > 3) are categorized as ligaments. This type of categorization has been utilized in previous studies and has shown a physical consistency [4,17].

3.2.1. Fragment velocity vs charge

The electrical force in a charged jet enhances its radial deflection,

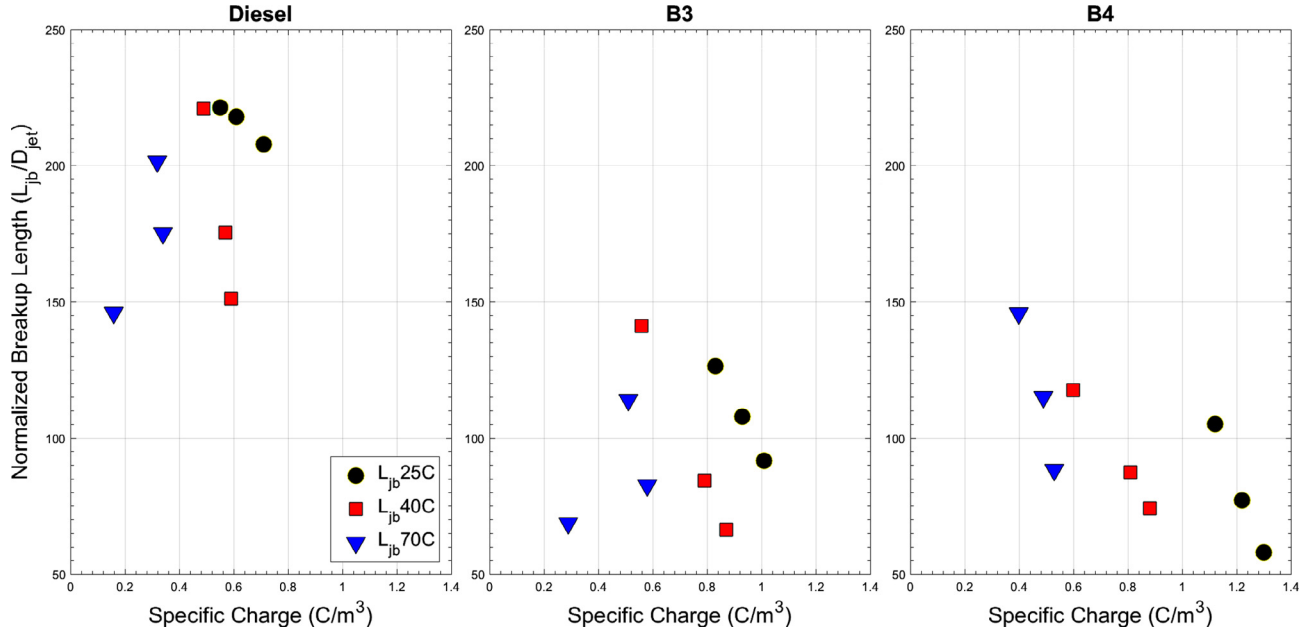

Fig. 9. Weighted mean of normalized jet breakup location for all three fuels vs specific spray charge for jet exit velocity of 10 m/s at normal temperature, 40 °C, and 70 °C.

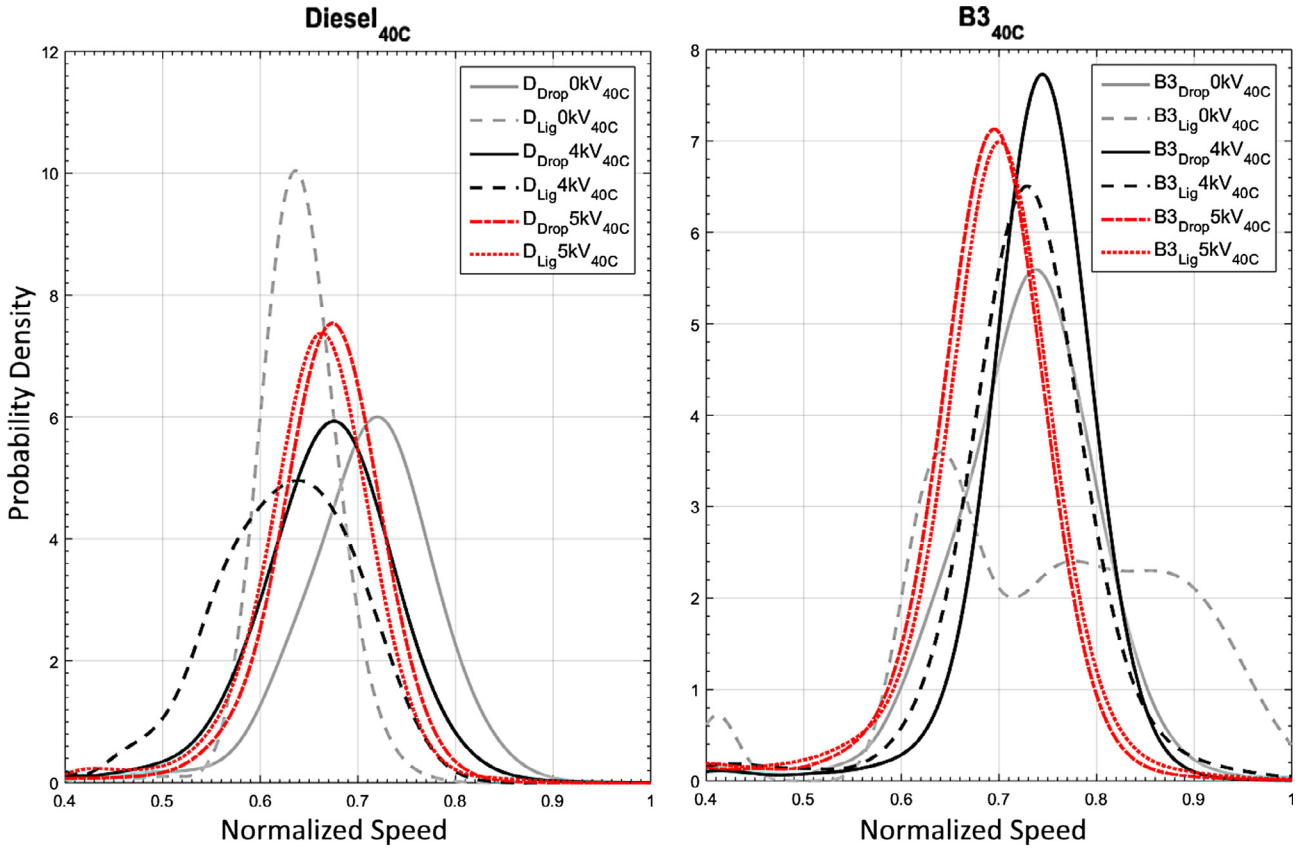

Fig. 10. Probability density distribution of normalized droplet velocity, and ligament velocity at two voltages for diesel and B3 fuel spray for a range of voltages. Left is the diesel spray at 40 °C and right is the B3 spray at 40 °C.

which could be formally quantified in terms of fragment velocity, both axial and radial. Fig. 10 shows the probability density distribution of droplets and ligament velocity normalized by the liquid jet exit velocity as a function of spray specific charge, for diesel and B3 sprays for a range of voltages at 40 °C. It is noticed that ligament velocity is very close to droplet velocity for all three fuels at 40 °C (only diesel and B3 are shown here for brevity). This behaviour is uncommon of air-blasted or pressurised atomizers, where the ligament velocity is, in general, low as compared to the droplet velocity, and this can also be observed through Fig. 10, given that the difference between droplet and ligament velocity is larger for the no voltage case compared to charged sprays. It is also noticed that with increase in voltage, the proximity between ligament velocity distribution and the droplet velocity distribution increases. This is likely due to the fact that in an electrostatic spray the jet flow governs the axial velocity and electrical force governs the radial velocity [5,8,7]. Therefore, with an increase in charge content, the radial dispersion of droplets increases and axial velocity decreases, which moves the axial velocity of a droplet closer to that of a ligament.

3.2.2. Normalized object count vs charge

The number density of fragments is an indicator of the quality of atomization. In previous studies, it has been used often to statistically analyse the atomization process [4]. Fig. 11 shows the normalized object count for all three fuels as a function of spray specific charge at normal temperature, 40 °C, and 70 °C. The object count is calculated by adding the total number of objects and normalizing by the total number of images (mean object per image). For all three fuel sprays at normal temperature and 40 °C, the total objects and droplet count increase with spray specific charge over the range measured. As expected, this indicates improved atomization at higher charge content.

At normal temperature, Fig. 11 suggests that the droplet concentration is higher for diesel sprays as compared biodiesel sprays, with the diesel spray also achieving a higher number density at low charge content as compared to other two fuels. The reason for this could be ascribed to the physical properties of the diesel. Among all tested fuels, the diesel has the lowest Ohnesorge number and highest Reynolds number, which promotes droplet formation [1,2,4]. An important observation that can be made from Fig. 11 is the significant increase in number density of droplets on preheating the biodiesel to 40 °C, for both B3, and B4. Heating the liquid reduces its viscosity, which promotes atomization, however, a further increase in temperature to 70 °C reduces the droplet concentration. This is most likely attributed to the lower specific charge at 70 °C, with a lower charge content decreasing the electrostatic atomization of the spray and resulting in lower droplet concentration. The same could be said for the diesel at 40 °C and 70 °C, where the droplet concentration is lower due to lower charge content. This implies that, to optimize the generation of droplets, a balance is required between the influence of preheating the fuel and the added charge.

The population of ligaments shows similar trends, where the ligament number density increases with spray specific charge for all fuels at normal temperature and 40 °C. Similar to droplet concentration trend, the object count for ligaments increases with preheating to 40 °C and reduces on further increase in temperature, as evident in Fig. 11.

3.2.3. Fragment size vs charge

The mean size of all the fragments, droplets and ligaments, for all three fuel sprays is presented in Fig. 12 and Fig. 13 vs. the spray specific charge for sprays at normal temperature, 40 °C, and 70 °C. The sizes are normalized by the jet diameter. At normal temperature, the object size, d10 (arithmetic mean diameter) of droplets and mean of major axis of ligaments seems to reduce slightly with an increase in spray specific charge, for each fuel. For instance the normalized d10 of Diesel at 25 °C decreases from 1.5 to 1.2, and similarly for B3 whereas B4 shows less of

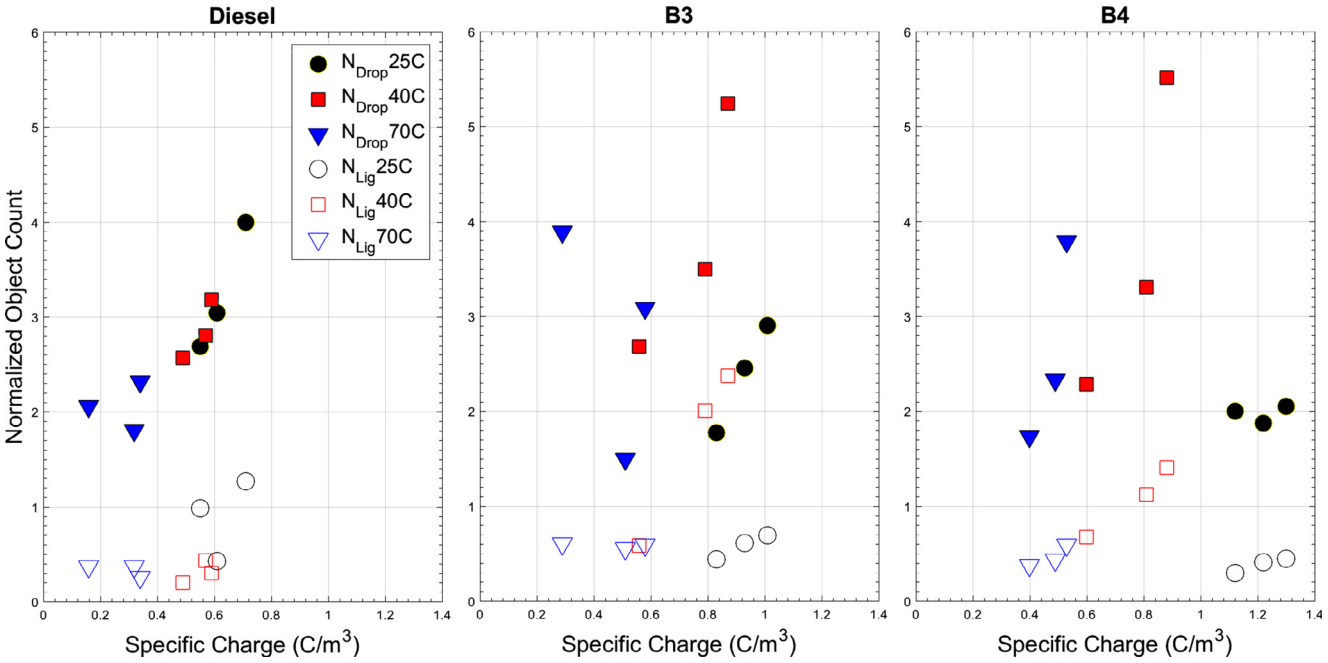

Fig. 11. Normalized object count of droplets and ligaments for all three fuels vs spray specific charge for spray with jet exit velocity of 10 m/s at normal temperature, 40 °C, and 70 °C. The object count is normalized by the number of images—it represents objects per image.

a significant change. It is important to note however that there is a limitation here in that the range of specific charge is narrow. Nevertheless, a similar trend for size is reported in previous studies by Shrimpton and Yule [15].

As discussed in the previous section, preheating a fluid reduces its viscosity and hence enhances atomization. Fig. 12 and Fig. 13 suggest that preheating the biodiesel to 40 °C results in lower object size for both droplets and ligaments, as expected. However, a further increase in temperature to 70 °C increases the mean object size for similar reasons as with the reduction in droplet concentration, i.e. the reduced electrostatic atomization at lower specific charge. Again, the same can be said for diesel sprays, where the object size increases with an increase in temperature due to lower charge content at higher temperature.

The behaviour of object number count and mean object size indicate a key feature of preheating fuel in electrostatic sprays, that the gain in atomization on preheating the fuel is limited by the charge content of the sprays. As discussed in the previous section, the reduced viscosity of the biodiesel at 40 °C enhances atomization due to favourable physical properties. However, the advantage of reduced viscosity is limited by the charge content of the spray—as a reduction in spray specific charge on further heating the fuel to 70 °C results in reduced electrostatic atomization. This suggests that preheating the high viscosity fuel is favourable for its atomization but limited by the increase in electrical conductivity of fuel at high temperatures.

3.2.4. Bimodal fragment size distribution

Figs. 14–16 show the loglog distribution of droplet size and

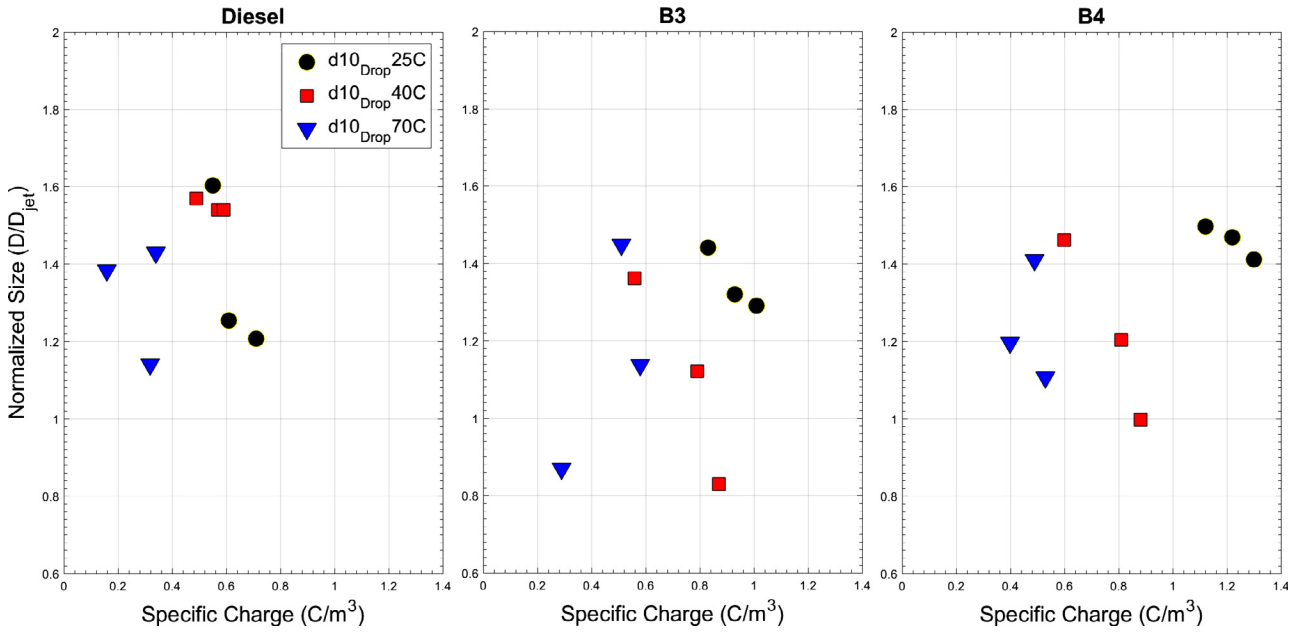

Fig. 12. Normalized droplet size for all three fuel sprays with jet exit velocity of 10 m/s at normal temperature, 40 °C, and 70 °C. 'd10' is the mean droplet diameter.

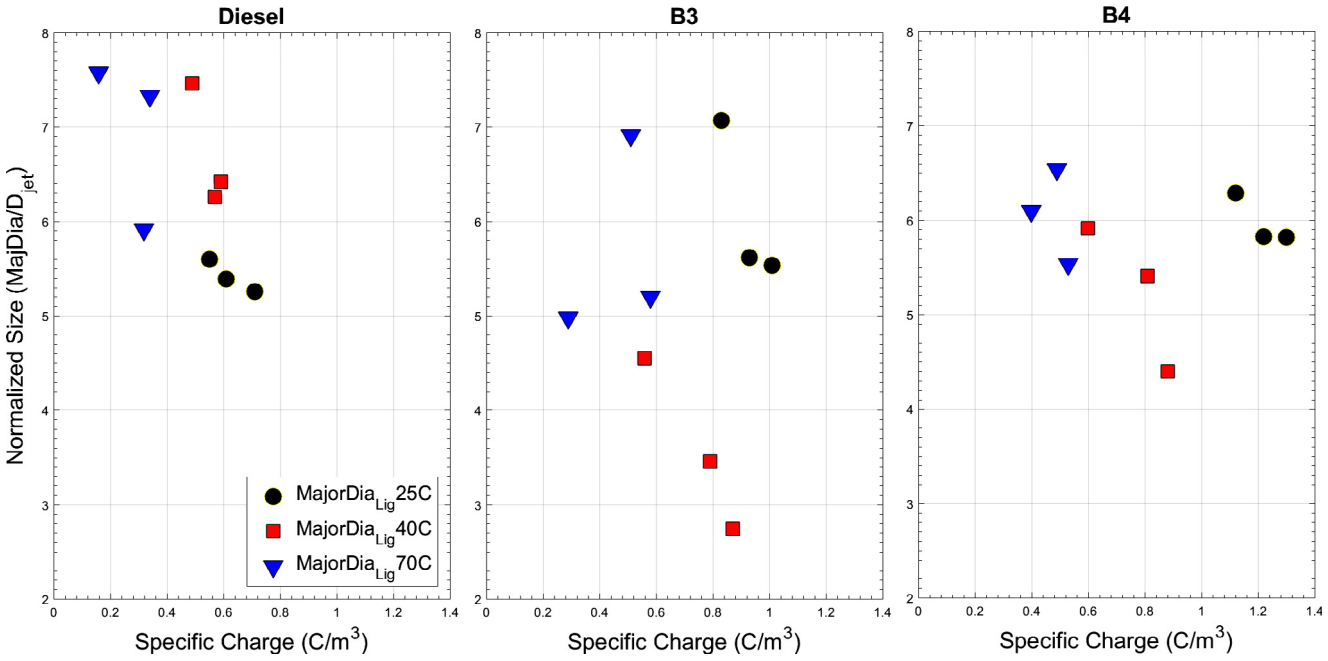

Fig. 13. Normalized ligament size for all three fuel sprays with jet exit velocity of 10 m/s at normal temperature, 40 °C, and 70 °C. 'MajDia' is the mean major axis of the ligaments.

ligament major axis plotted for diesel, B3, and B4 sprays for two voltages—for diesel and B3, where the right side plot is at the critical voltage. The plots for diesel are at 25 °C, and those for B3, and B4 are at 40 °C. It is evident that below the critical voltage the droplet size follows a bimodal distribution for all three fuels and this is consistent with the literature on electrostatic sprays [5,7,15]. The first peak appears at a normalized size (size/liquid jet diameter) close to 0.5. The second and larger peak appears at a normalized size close to 2, which is consistent with the droplet size that would be expected in Rayleigh breakup [2,1]. Also, with an increase in voltage, the peak of the larger droplets shifts toward the lower size owing to better atomization at higher charge content. The same is evident in Fig. 12, where the d10 of the droplets decreased with increase in spray specific charge.

The distribution of droplet size suggests an important feature of the electrostatic sprays that an increase in charge content supresses the bimodality. It is evident in all three figures, 14, 15, 16, that an increase in voltage, which increases the charge content of spray, increases the number density of droplets corresponding to the entire size spectrum.

3.3. Use of local non-dimensional numbers

The velocity obtained by the high-speed imaging technique can be used to calculate non-dimensional parameters for each individual object, especially the local Weber number, as opposed to overall global dimensionless numbers. Local dimensionless numbers can provide a much more detailed description of the state of the spray as opposed to a global analysis, and this has been demonstrated elsewhere [7,2,1,18]. Here, an effective surface tension is used to account for the liquid charge content, using Eq. (2). The definition of effective surface tension as applied to liquid jets may be found in Kourmatzis et al. [7].

$$\sigma_l^* = \sigma_l - \frac{Q_v^2 d^3}{48\varepsilon_0} \tag{2}$$

Here, σ is the surface tension of the liquid, Q_v is the spray specific charge in C/m^3, d is the jet diameter, ε_0 is the relative permittivity of the liquid. For diesel, a relative permittivity of 2.2 is used for calculation [16]. The local Weber number is calculated using this effective surface tension.

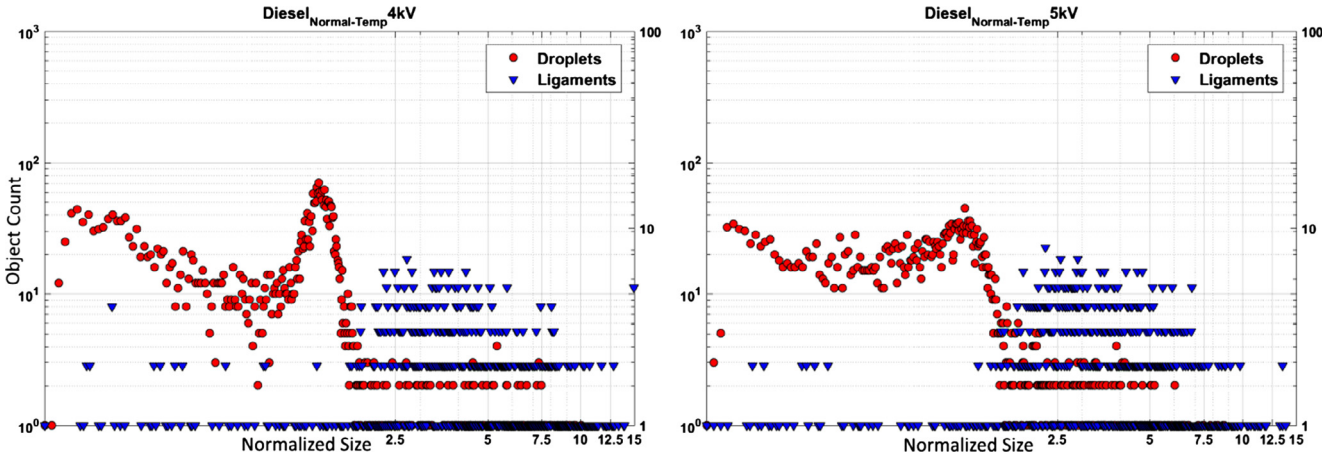

Fig. 14. Logarithmic distribution of droplet and ligament size at two voltages for diesel spray with jet exit velocity of 10 m/s at normal temperature.

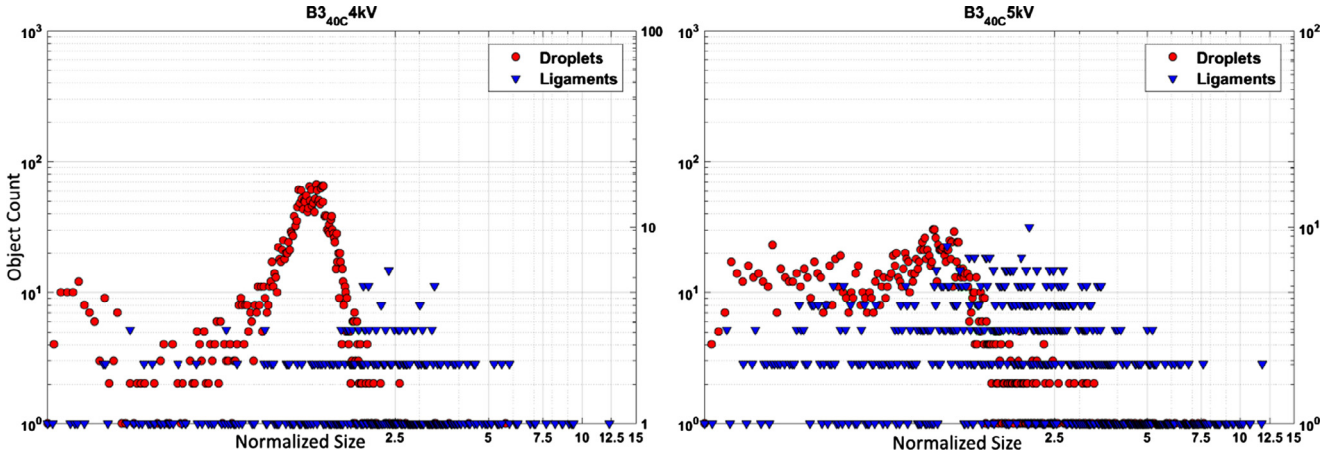

Fig. 15. Logarithmic distribution of droplet and ligament size at two voltages for B3 spray with jet exit velocity of 10 m/s at 40 °C.

3.3.1. Local Weber number vs size

The definition of local Weber number includes air density (ρ), slip velocity (U_s), surface tension (σ) and characteristic dimension of object (D_c) as shown in Eq. (3).

$$We_{local} = \frac{\rho U_s^2 \times D_c}{\sigma} \quad (3)$$

In the downstream region, the droplet diameter is used as D_c to calculate local Weber number, which is a reasonable assumption as most of the objects are droplets. However, in the upstream or near-field region, the use of droplet diameter introduces uncertainties due to the presence of ligaments and irregular objects. Shinjo et al. [19], in their DNS work, used the semi-minor axis of the fragments as the characteristic length-scale to calculate local Weber number, and we adopt this same approach for consistency. We also adopt the definition of Shinjo and Umemura [19] for the local Weber number as follows:

$$We_{local} = \frac{\rho(U_{frag} - U_{gas})^2 \times a}{\sigma^*} \quad (4)$$

Here, We_{local} is the Weber number, ρ is the density of air, U_{frag} and U_{gas} is the velocity of fragment and gas, respectively, σ* is the effective surface tension of the fuel and 'a' is the semi minor axis of the fragment.

Fig. 17 shows the square root of local Weber number vs. major axis of objects for a range of applied voltages. The horizontal red line, $We_{local}^{0.5} = 0.8$, indicates the threshold where the ratio of local aerodynamic force and surface tension is comparable to induce fragment breakup [18,19,29]. Here it is noticed that, for the critical voltage location, the square root of local Weber number for larger fragments approaches the transition value of $We_{local}^{0.5} = 0.8$ also reported by Shinjo et al. [19], which is in further agreement with the results of Umemura et al. [29] and Pham et al. [18].

For low Weber number cases (We < 1), this value indicates the transition of the liquid jet from jetting to dripping and it is noticed that an increase in specific charge shifts the square root of local Weber number towards $We_{local}^{0.5} = 0.8$. This not only indicates that an increase in charge content enhances the probability of spray atomization, but also highlights the near universality in the relevance of this critical local Weber number. This threshold has now been confirmed for laminar jet dripping mode breakup [29], ligament atomization in highly turbulent sprays [19] (where the ligament is modelled as a laminar liquid jet), ligament atomization in air assisted sprays [18], and here for electrified laminar liquid jets at the critical charge level.

4. Conclusions

Time resolved near-field spray characteristics are studied using high speed imaging and particle tracking velocimetry. Image processing, using a validated method, is employed to obtain the flow characteristics of the portions of the spray which are not normally resolvable using standard droplet size and velocity measurement techniques such as phase Doppler anemometry and laser diffraction. General features of specific charge and spray bimodality are in agreement with previous work. However, this contribution extends the existing literature by providing local spray characteristics such as arbitrarily shaped fragment population, spray dispersion, and fragment velocity to understand the relation between electrical performance and spray characteristics.

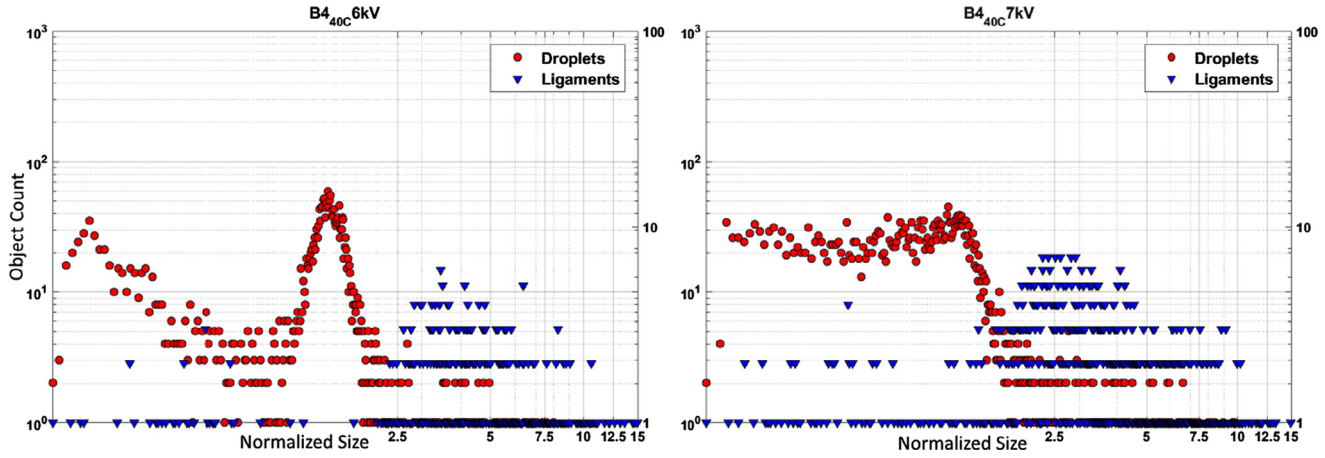

Fig. 16. Logarithmic distribution of droplet and ligament size at two voltages for B4 spray with jet exit velocity of 10 m/s at 40 °C.

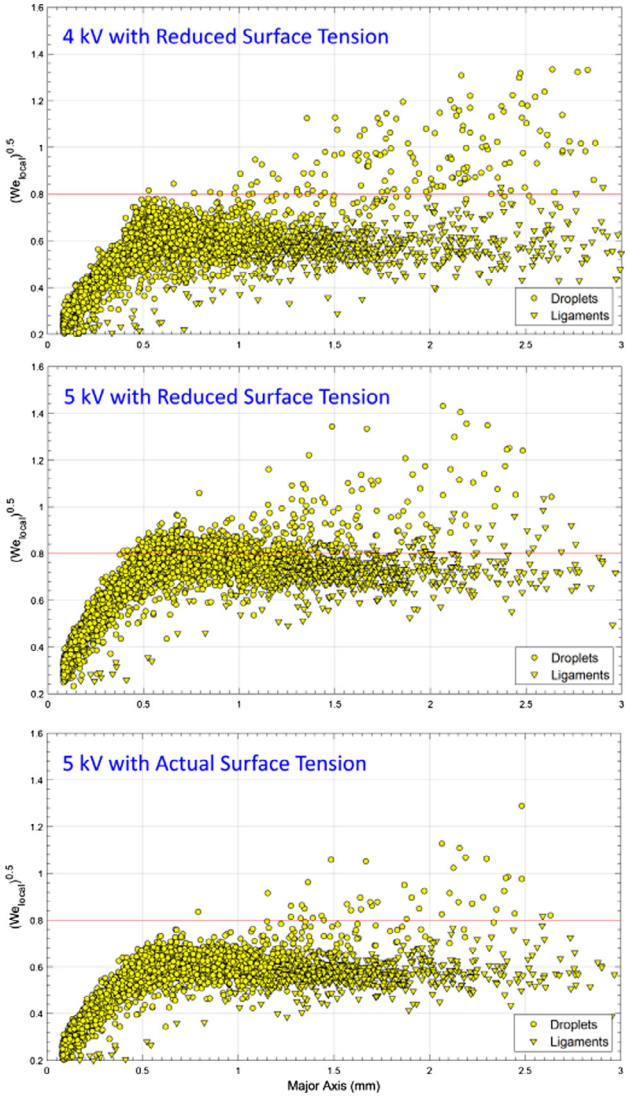

Fig. 17. Square root of local Weber number vs the major axis of fragments for diesel at various applied voltages for sprays with jet exit velocity of 10 m/s. From top to bottom: 4 kV and 5 kV with reduced surface tension, and 5 kV with actual surface tension.

These techniques are applied to sprays with varying applied potential and varying temperatures. With the availability of localized near-field data, local dimensionless characteristics of the objects were also studied for the first time, with a local Weber number using an effective surface tension term. The main conclusions from the study are listed below.

- The droplet number density increases with specific spray charge, for all three fuels, however diesel indicates a large population of atomized fragments compared to other fuels.
- Preheating the high viscosity fuel enhances the spray atomization and results in higher droplet concentration, which has smaller size as compared to droplets produced at normal temperature.
- There is a reduction in spray specific charge with an increase in temperature, and therefore there is a balance between the influence viscosity, and charge on atomization.
- The fragment and jet orientation changes significantly with an increase in charge content.
- The local Weber number increases with an increase in charge content and the square root of local Weber number is closest to a transition threshold of 0.8 at the critical voltage, in agreement with previous work in laminar liquid jet and ligament atomization for uncharged sprays, showing a degree of universality in the atomization process.

Acknowledgments

The work is funded by the Australian Research Council.

References

[1] Dumouchel C. On the experimental investigation on primary atomization of liquid streams. Experim Fluids 2008;45:371–422.
[2] Faeth GM, Hsiang L-P, Wu P-K. Structure and breakup properties of sprays. Int J Multiph Flow 1995;21:99–127.
[3] Kourmatzis A, Pham PX, Masri AR. Characterization of atomization and combustion in moderately dense turbulent spray flames. Combust Flame 2015;162:978–96.
[4] Lowe A, Kourmatzis A, Masri AR. Turbulent spray flames of intermediate density: Stability and near-field structure. Combust Flame 2017;176:511–20.
[5] Shrimpton J. Charge injection systems: physical principles, experimental and theoretical work. Berlin Heidelberg: Springer; 2009.
[6] Kourmatzis A, Shrimpton JS. Electrohydrodynamic inter-electrode flow and liquid jet characteristics in charge injection atomizers,. Experim Fluids 2014;55:1688.
[7] Kourmatzis A, Ergene EL, Shrimpton JS, Kyritsis DC, Mashayek F, Huo M. Combined aerodynamic and electrostatic atomization of dielectric liquid jets. Experim Fluids 2012;53:221–35.
[8] Malkawi G, Yarin AL, Mashayek F. Breakup mechanisms of electrostatic atomization of corn oil and diesel fuel. J Appl Phys 2010;108:064910.
[9] Shrimpton JS, Rigit ARH. Spray characteristics of charge injection electrostatic atomizers with small-orifice diameters. Atomization Sprays 2006;16:421–42.
[10] Ciach T. Application of electro-hydro-dynamic atomization in drug delivery. J Drug Delivery Sci Technol 2007;17:367–75.
[11] Didion J. STP-H5-Electro-Hydro Dynamics (STP-H5 EHD), NASA Space Mission.
[12] Pareta R, Edirisinghe MJ. A novel method for the preparation of starch films and coatings. Carbohydr Polym 2006;63:425–31.
[13] Agathou MS, Kyritsis DC. Electrostatic atomization of hydrocarbon fuels and bio-alcohols for engine applications. Energy Convers Manage 2012;60:10–7.
[14] Anderson EK, Kyritsis DC, Carlucci AP, Risi AD. Electrostatic effects on gasoline direct injection in atmospheric ambiance. Atomization Sprays 2007;17:289–313.
[15] Shrimpton JS, Yule AJ. Characterisation of charged hydrocarbon sprays for application in combustion systems. Experim Fluids 1999;26:460–9.
[16] Al-Ahmad G, Shrimpton JS, Ergene EL, Mashayek F. Electrical performance of a charge-injection atomizer using viscous organic oils. Atomization Sprays 2009;19:547–66.
[17] Kourmatzis A, Pham PX, Masri AR. A two-angle far-field microscope imaging technique for spray flows. Meas Sci Technol 2017;28:035302.
[18] Pham PX, Kourmatzis A, Masri AR. Local characteristics of fragments in atomizing sprays. Exp Therm Fluid Sci 2018;95:44–51.
[19] Shinjo J, Umemura A. Simulation of liquid jet primary breakup: dynamics of ligament and droplet formation. Int J Multiph Flow 2010;36:513–32.
[20] Singh G, Singh AP, Agarwal AK. Experimental investigations of combustion, performance and emission characterization of biodiesel fuelled HCCI engine using external mixture formation technique. Sustainable Energy Technol Assess 2014;6:116–28.
[21] Rahman MM, Pourkhesalian AM, Jahirul MI, Stevanovic S, Pham PX, Wang H, et al. Particle emissions from biodiesels with different physical properties and chemical composition. Fuel 2014;134:201–8.
[22] Gorty AV, Barringer SA. Electrohydrodynamic spraying of chocolate. J Food Process Preserv 2011;35:542–9.
[23] Pham PX, Kourmatzis A, Masri AR. Simultaneous volume-velocity measurements in the near field of atomizing sprays. Meas Sci Technol 2017;28:115203.
[24] Ahmed T, Kourmatzis A, Pham PX, Masri AR. Droplet evaporation modeling of electrified fatty acid methyl esters. Fuel 2018;231:244–52.
[25] Kourmatzis A, Pham PX, Masri AR. Air assisted atomization and spray density characterization of ethanol and a range of biodiesels. Fuel 2013;108:758–70.
[26] Palaniappan Sevugan, Sastry Sudhirk. Electrical conductivity of selected juices: influences of temperature, solids content, applied voltage, and particle size. J Food Process Eng 1991;14:247–60.
[27] Chhetri AB, Watts KC. Surface tensions of petro-diesel, canola, jatropha and soapnut biodiesel fuels at elevated temperatures and pressures. Fuel 2013;104:704–10.
[28] Das M, Sarkar M, Datta A, Santra AK. Study on viscosity and surface tension properties of biodiesel-diesel blends and their effects on spray parameters for CI engines. Fuel 2018;220:769–79.
[29] Umemura A. Self-destabilizing mechanism of a laminar inviscid liquid jet issuing from a circular nozzle. Phys. Rev. E 2011;83(4). p. 046307.
[30] Kourmatzis A, Shrimpton JS. Electrical and transient atomization characteristics of a pulsed charge injection atomizer using electrically insulating liquids. J Electrostat 2011;69:157–67.
[31] Vesely PW, Schick RJ, Shrimpton JS, Mashayek F. Energy efficient primary atomization of viscous food oils using an electrostatic method. J Food Eng 2018;237:27–32.
[32] Mekonen MW, Sahoo N. Effect of fuel preheating with blended fuels and exhaust gas recirculation on diesel engine operating parameters. Renewable Energy Focus 2018;26:58–70.